International Journal of Solids and Structures 315 (2025) 113349

Contents lists available at ScienceDirect

International Journal of Solids and Structures

journal homepage: www.elsevier.com/locate/ijsolstr

Rescaling and mesoshear deformations of lattice metamaterials

M. Spagnuolo [a,b,*], V.A. Eremeyev [a,b], F. D'Annibale [b,c], F. Hild [d]

[a] DICAAR (Dipartimento di Ingegneria Civile, Ambientale e Architettura), University of Cagliari, Italy
[b] M&MoCS (International Research Center for the Mathematics and Mechanics of Complex Systems), University of L'Aquila, Italy
[c] DICEAA (Dipartimento di Ingegneria Civile, Edile - Architettura, Ambientale), University of L'Aquila, Italy
[d] Université Paris-Saclay, CentraleSupélec, ENS Paris-Saclay, CNRS, LMPS–Laboratoire de Mécanique Paris-Saclay, Gif-sur-Yvette, France

ARTICLE INFO

Keywords:
Lattice Metamaterials
Rescaling
Generalized Continuum Mechanics
Mesoshear deformation
Fibrous architecture

ABSTRACT

Experimental results are presented for a lattice metamaterial with a complex mesostructure composed of parallel fibers aligned at different levels. The experimental evidence suggests that the fibers, in addition to their own deformations, such as elongation and bending, and to the relative rotation between two adjacent layers, may also slide relative to each other under certain conditions. This deformation mechanism is taken into account and used as a key hypothesis in the development of a new continuum model. A remarkable rescaling property possessed by the considered metamaterial is also discussed.

1. Introduction

In the study of newly developed materials, an emerging approach is crucial, namely, that based on the design and the synthesis of mesostructures (which, depending on the scientific milieu one belongs to, may also be referred to as architecture or mesoarchitecture). It has been observed in recent years that a profitable search for new materials with mechanical (and other) properties that are more efficient than those of what are commonly called natural materials cannot ignore their internal geometry. This feature was already clear in the 1970s (see P. Germain's pioneering work (Germain, 2020) or R. Mindlin's work on microstructures (Mindlin, 1965)), but today it is favored over, for example, chemical research by the generalization of production technologies based on additive manufacturing (Leonardi et al., 2024).

The fact that the mesostructure of a material influences its mechanical properties is well known. If one refers to the crystal lattice of a solid medium, it is known that diamond and graphite, although formed from the same carbon atoms, differ significantly due to the different positioning of the atoms. The innovation comes when a qualitative leap is made and the meaning of the term mesostructure is extended. Even today, some scientists prefer to use different terminologies when referring to materials whose mesostructure is not at such a deep level as the crystal lattice. In reality, the idea is exactly the same, namely, to introduce a basic quantity, which is actually called elementary cell, and with this element to construct a mesostructure which, once homogenized, produces a continuum endowed with certain properties that depend directly on the geometry of the chosen microstructure.

Paul Germain's insight was that certain mesostructures, when homogenized, gave rise to continua described by second gradient theories. Such theories are capable of modeling materials with extremely exotic mechanical properties. With the advent of additive manufacturing and 3D printing, it is now possible to produce samples with complex mesostructures that are theoretically described by second gradient continuum models. Specifically, this idea was first presented by Alibert et al. (2003) and Seppecher et al. (2011), where the so-called pantographic beam was introduced as a one-dimensional continuum material described by a second gradient in-extensional strain energy. This model was later extended (dell'Isola et al., 2016), where the synthesis of a pantographic sheet was shown.

The mechanical response of pantographic metamaterials is shown to be strongly dependent on material anisotropy and scaling, particularly when fiber arrangements vary or are non-uniform. As shown by Giorgio et al. (2024), introducing second-grade elasticity for three-dimensional lattices highlights the sensitivity of overall stiffness to both the orientation and arrangement of fibrous elements. Mesoscopic offsets and relative rotations in two-layer pantographs are shown to be responsible of substantially altering deformation patterns (Giorgio et al., 2021), revealing how geometric scaling strongly influences global behavior. Meanwhile, Giorgio (2021) illustrates how distinct fiber configurations in lattice shells lead to markedly different outcomes in topology optimization, underscoring the importance of careful design to leverage anisotropy advantages. It is then clear that a nuanced understanding of material anisotropy and scaling is essential for tailoring the mechanical properties of pantographic structures.

Such a material has mechanical properties that are directly related to the geometry of the mesostructure, and the deformation properties

* Corresponding author at: DICAAR (Dipartimento di Ingegneria Civile, Ambientale e Architettura), University of Cagliari, Italy.
E-mail address: mario.spagnuolo@unica.it (M. Spagnuolo).

https://doi.org/10.1016/j.ijsolstr.2025.113349
Received 23 November 2024; Received in revised form 1 March 2025; Accepted 18 March 2025
Available online 2 April 2025

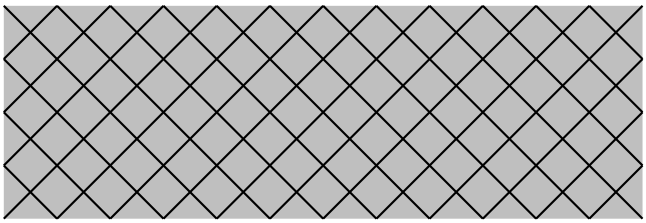

Fig. 1. Schematic geometry of a pantographic sheet made of two families of fibers.

of the constituents of the elementary cell. A pantographic lattice is composed of at least two layers of fibers arranged parallel to each other at each level, the layers belonging to planes that are themselves parallel to each other. Each layer of fibers has its own orientation, and between one layer and another the orientation must be different. Generally the layers are constructed so that the fibers in one layer are oriented orthogonally to those in the adjacent one (Fig. 1). The fiber layers need to be joined together to allow them to interact. The connections between the fiber layers, mathematically described as fiber families, are implemented in a variety of ways. Depending on the type of analysis and the type of model to be adopted, different interconnections are considered.

Dynamic analyses play a pivotal role in uncovering the rich mechanical behavior of pantographic metamaterials, particularly when investigating phenomena such as wave propagation and boundary layer effects. This perspective has been highlighted in recent research (Laudato et al., 2022), where large-strain experiments illuminate the influence of boundary layers on the overall structural response. Likewise, the importance of modeling wave transmission to capture the intricate deformation patterns unique to these advanced materials is shown by Ciallella et al. (2022a). These studies demonstrate that a dynamic viewpoint is indispensable for deepening the understanding of pantographic metamaterial systems.

This study investigates the mechanical behavior of lattice metamaterials characterized by complex mesostructures, specifically parallel fibers arranged on multiple levels. By conducting bias extension tests on three different pantographic block specimens (Section 2.1), the key deformation mechanisms include elongation, bending, and relative sliding between fiber layers. These observations are instrumental in developing a new continuum model that accurately represents the material behavior. The present findings highlight the significant impact of hinge height on the material response. By normalizing the measured forces by the total number of hinges (Section 2.2), a dependence of the material behavior on the hinge height is proven. Additionally, it is shown that mesoshear deformation, caused by relative sliding between fiber layers, is more pronounced in specimens with taller hinges (Section 2.3). A Poisson-like transverse effect is also noted, particularly in specimens with slender hinges (Section 2.4). To effectively capture these phenomena, a second gradient continuum model is introduced (Section 3). This model integrates terms for fiber elongation, bending, and hinge torsion, thereby providing a comprehensive representation of the mechanical response of the studied metamaterial. Numerical simulations are performed to calibrate the constitutive parameters (Section 4), and the results demonstrate strong agreement with experimental data, confirming the model validity.

In summary, this research underscores the crucial role of mesostructural geometry in determining the mechanical properties of lattice metamaterials. The developed continuum model, which accounts for second gradient effects and mesoshear deformation, offers a robust framework for predicting the behavior of such materials under various loading conditions.

2. Experimental evidences and phenomenological hypotheses

2.1. Experimental setting and results

Three different types of pantographic blocks were subjected to a bias extension test. The three types of specimens differed in the geometric characteristics of the mesostructure, but had the same material characteristics. More specifically, the dimensions of the fiber cross-section and the radius of the cylinders used to connect the various layers of fibers coincided for all three specimens, while the cylinder height and the fiber density per layer differed. Let us denote 3_w, 2_w and 2_d as these three types, whose geometrical properties are given in Table 1.

In Fig. 2 the main geometrical features of the pantographic blocks are reported. In Fig. 2a, the quantities associated with fiber density are defined. If a is the fiber width and d the interdistance between fibers of the same family, then λ_a and λ_d are the projections of these quantities on the short side of the structure, whose length is ℓ. Fig. 2b shows the macroscopic quantities of the pantographic block, namely, ℓ and L the lengths of the base, and H the height. Last, Fig. 2c defines the dimensions of the fibers, with a and b the base and height of the fiber cross-section respectively, and of the cylinders connecting the fibers, where h is the height and $2r$ the diameter of the cylinder.

There are two fundamental differences between the studied architectures. Specimen 3_w has a hinge height of 3 mm and an interdistance between the fibers of 1.6 mm; specimen 2_w has the same interdistance between the fibers, but hinges 2 mm in height; specimen 2_d has hinges 2 mm in height, and an interdistance between the fibers of 0.7 mm. The resulting grid is displayed in Fig. 3 for the top views of the three types of specimens.

Fig. 4 shows lateral views of all of them. It was decided to simultaneously acquire photographs of the upper and lateral faces of the pantographic block in order to visualize the different deformation mechanisms involved in the behavior of the metamaterial. For the upper face, one observes bending and elongation of the fibers, while for the lateral face, torsion and shear of the cylinders occurred, which is called mesoshear to differentiate it from macroscopic shear. This type of information can also be analyzed experimentally in detail using Digital Image Correlation techniques (Hild and Roux, 2012; Tomicevic et al., 2013; Hild et al., 2021).

The bias extension tests conducted on the three types of specimens returned three results for each acquisition step:

i. the applied force;
ii. a photo of the top view;
iii. and a photo of the lateral view.

As shown later on, the lateral view is crucial in checking a hypothesis that will be introduced to explain the observed phenomenology. Fig. 5 displays the three plots of the measured force versus prescribed displacement. The three curves are similar in shape (*i.e.*, the mechanical response is determined by the mesostructure, which is the same) but different in levels. The differences are attributed to two factors, namely, the height of the hinges and the number of fibers. It is worth pointing out that, rather than the number of fibers, it is the number of hinges that counts. As earlier reported (Spagnuolo et al., 2021), the mechanical behavior of a pantographic metamaterial should not depend on the number of fibers, since its mesostructure induces effects proper to second gradient continua, even in the presence of low fiber densities.

2.2. Hinge-dependence of the metamaterial response

The three curves representing the applied force in relation to the prescribed displacement have similar trends, but do not coincide (Fig. 5). For the two pantographic blocks with different hinge heights, it is due to that difference. For the two blocks having the same hinge geometry, one should observe an almost superimposable curve. It was

Table 1
Geometrical properties of the three types of samples.

Sample	n_f	h (mm)	r (mm)	a (mm)	b (mm)	ℓ (mm)	L (mm)	H (mm)
3_w	15	3	0.5	1.0	1.5	70	210	29.5
2_w	15	2	0.5	1.0	1.5	70	210	29.5
2_d	20	2	0.5	1.0	1.5	70	210	37.5

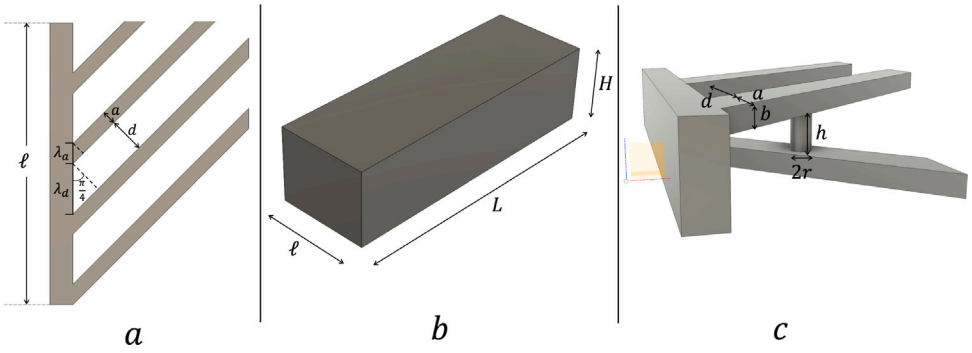

Fig. 2. Relevant geometrical parameters of the studied metamaterials. (a), (c) Characteristics at the fiber scale; (b) characteristics at the specimen scale.

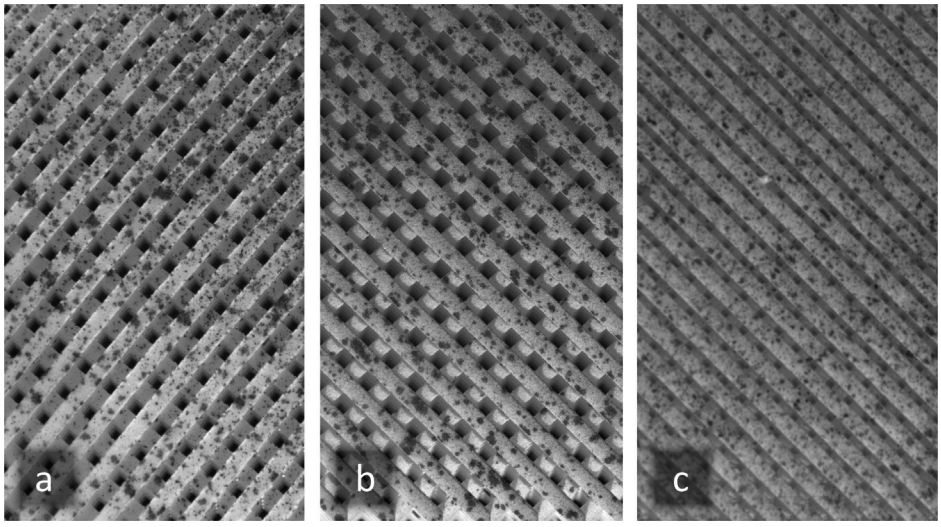

Fig. 3. Top view of the central zones of the three types of specimens before testing. (a) 3_w, (b) 2_w and (c) 2_d. Speckle patterns are observed, which were introduced for registering the pictures via Digital Image Correlation (Hild and Roux, 2012; Tomicevic et al., 2013; Hild et al., 2021).

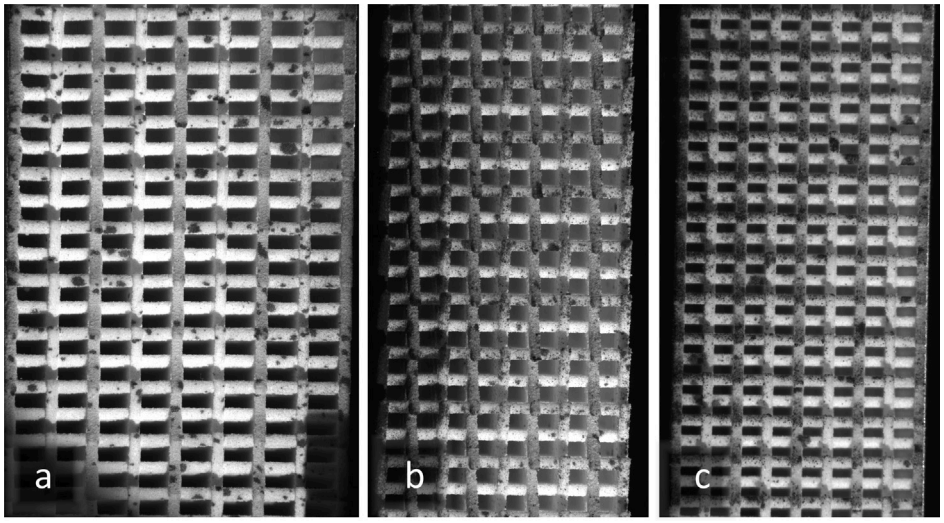

Fig. 4. Lateral view of a portion of the three types of specimens before testing. (a) 3_w, (b) 2_w and (c) 2_d.

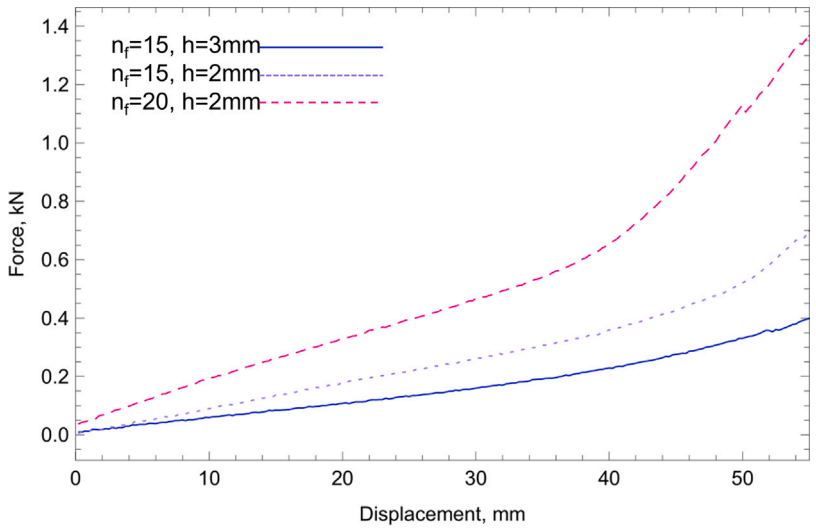

Fig. 5. Applied force versus prescribed displacement for the three types of studied specimens.

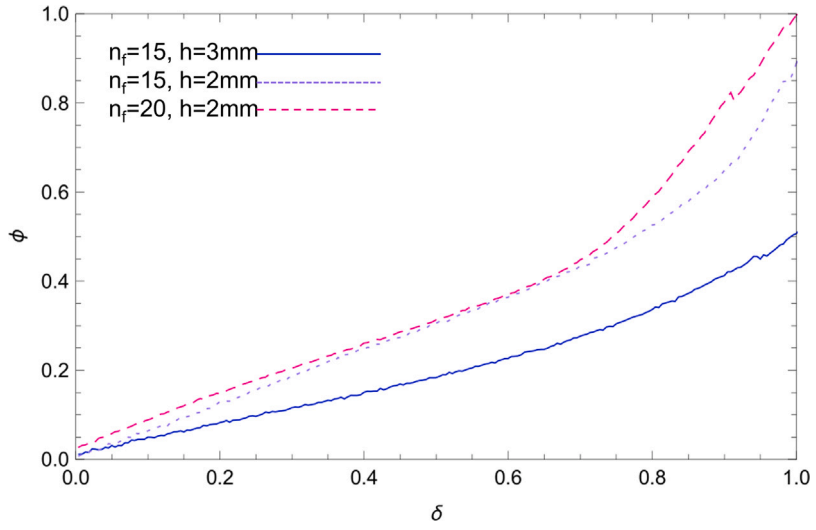

Fig. 6. Rescaled force versus dimensionless displacement for the three specimens. It is noted that, after rescaling, the curves relative to geometries with their hinge height equal to 2 mm fully coincide in the first part of the test.

observed (Spagnuolo et al., 2021) that a homogenized continuum model can also be used to interpret experimental tests carried out on loose network samples. The presence of the architecture influences the mechanical response of the metamaterial, even if it cannot properly be considered as a continuum.

The problem lies in the fact that the hinges are responsible for most of the deformation observed in pantographic metamaterials. If the fibers are only slightly bent and almost not stretched during a tensile test, the hinges are subjected to non-negligible torsion and, by increasing their number, they also significantly increase the total strain energy of the specimen. To make the experimentally observed quantities independent of the number of hinges, one may proceed by dividing the measured forces by the total number of hinges. This operation yields a rescaled force, which at this point should only depend on the height of the hinges. Fig. 6 shows that the two curves corresponding to the pantographic blocks with the same hinge height almost coincide, which is different for the other sample.

Another small difference is observed between the curves characterizing the two pantographic blocks 2_w and 2_d. This difference occurs in the last part of the tensile test and is again attributed to the different number of fibers characterizing the two specimens. This time, the problem is not so much that a greater number of fibers may generate a higher amount of strain energy than in the specimen with fewer fibers, but rather that the two specimens reach fiber contact at two different instants of time. In the specimen with more fibers, contact between the fibers occurred earlier and this consequently induced the inception of the hardening phase of the specimen. Stretching a fiber is less energetically favorable than bending it, which is why the force measured for the 2_d specimen is greater than the other two. This feature is discussed in more detail in the next section, where a suitable model is introduced to describe the behavior of the tested specimens.

In Fig. 7, the evolution of the central part of the upper face of specimen 3_w is shown. This image explains how, in the central area of the upper face, the fibers mostly rotated. Bending of the fibers is concentrated at the interface between this central zone and the quasi-rigid zones where the fibers are clamped at the short side.

2.3. Role of mesoshear

The difference between the force–displacement curves observed for the pantographic blocks is due to the only geometric parameter that differentiates them, namely, the height of the hinges. The observed

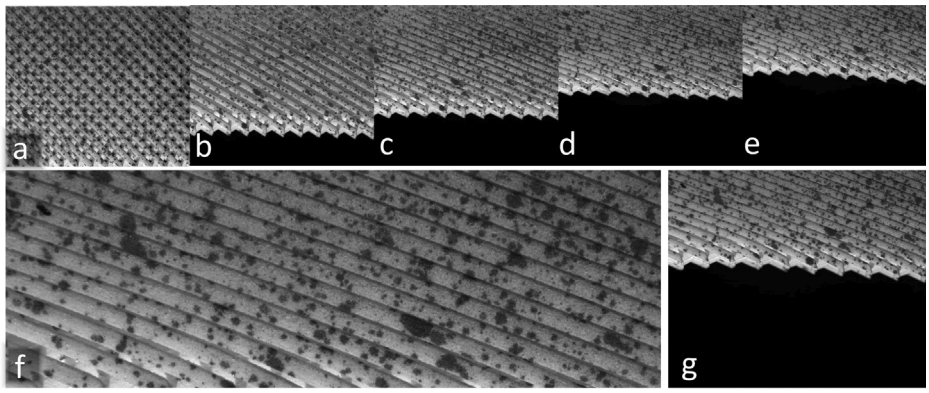

Fig. 7. Top face views of specimen 3_w. The central part of the top face is shown along the deformation for selected steps (a-e). Enlarged image (e) at a larger scale (f) and smaller scale (g) to show that in the central zone of the specimen the fibers mostly rotated. Bending occurred at the interface between the central and lateral zones.

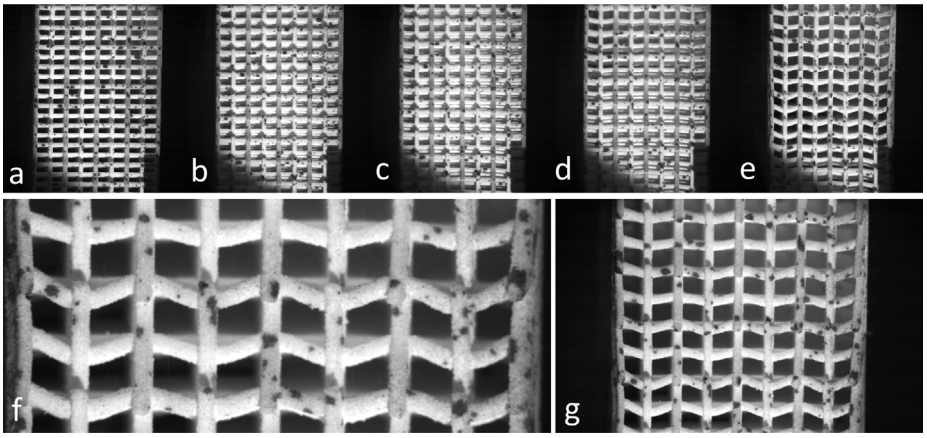

Fig. 8. Lateral face of specimen 3_w. The lateral face is shown, for its part near the short side of the block, along the deformation for selected steps (a-e). Enlarged image (e) at a larger scale (f) and smaller scale (g) to show that near the short side of the specimen mesoshear of cylinders is non negligible.

phenomenology is interpreted by considering the two systems as differentiated by their number of degrees of freedom. It is well-known that slender beams are more deformable than bulky ones (Spagnuolo et al., 2017), which leads us to consider that in the case of the specimen with longer hinges, the latter ones are not only twisted due to the relative rotation between the fibers of the two planes, but are also sheared due to a relative motion between the fiber planes. This phenomenon of "sliding" is well known in textiles, where the fibers are simply held together by the warp (Nadler and Steigmann, 2003; dell'Isola and Steigmann, 2015; Steigmann and dell'Isola, 2015). In the present case, the fibers are held together by the hinges, which also act as a constraint on the relative displacements. When the aspect ratio of the hinges becomes much greater than 1, the constraint is relaxed and relative displacements are allowed. In Fig. 8, the part of the lateral face that is near the short side of the pantographic block is shown for specimen 3_w. In that part, as it has been shown by numerical simulations and experimental tests published in the literature, the sliding of the fibers, and therefore mesoshear of the connecting cylinders, is concentrated. The mesoshear deformation is shown through pictures corresponding to different deformation steps, and it is concluded that this deformation mechanism cannot be disregarded in the modeling of this metamaterial, at least when the cylinders are slender.

The relaxation of this kinematic constraint, which prevents sliding between the fiber planes, introduces a new deformation mechanism (Spagnuolo et al., 2017; Andreaus et al., 2018), which is more advantageous at a certain stage in the tensile test of the pantographic block. For the same total elongation of the specimen, in the case of sample 3_w, less bending of the fibers is observed with respect to mesoshear (*i.e.*, shear of the hinges), which is not observed for specimen 2_w. It may therefore appear that mesoshear is favored over fiber bending. This statement is actually not correct, as only the sliding mechanism is favored over shear of the hinges. It is interesting to note that mesoshear is favored over macroshear, which, as will be seen, corresponds to torsion of the hinges.

2.4. Transverse depth reduction estimate: A Poisson-like effect

With reference to Fig. 9, it is assumed that after a pretensioning test of the pantographic block, some areas experience transverse contraction. This contraction, which is not always observable but depends on the geometric features of the pantographic metamaterial, turns out to be a discrete Poisson effect or, more appropriately, a Poisson-like effect; contraction in the transverse direction is observed after stretching the sample.

The magnitude of this Poisson effect is estimated from geometric considerations. It is closely related to mesoshear of the hinges. For pantographic blocks containing hinges with a thick aspect ratio, this effect will be absent or negligible. As a first approximation, after introducing the angle ϑ (Fig. 9), it is observed that $\mathrm{h}^* = \mathrm{h}\cos(\vartheta)$. Moreover, the height H is the sum of the widths of the single pantographic fiber layers, and the height of the hinges multiplied by the number of fiber layers minus one

$$H = n\ b + (n-1)\ \mathrm{h} \tag{1}$$

Similarly, the height H^* reads

$$H^* = n\ b + (n-1)\ \mathrm{h}^* \tag{2}$$

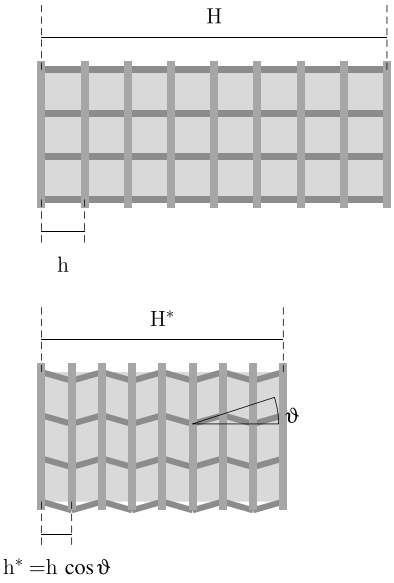

Fig. 9. Poisson-like effect. Due to mesoshear of connecting hinges, the interdistance between pantographic layers changes, thereby resulting in transverse contraction.

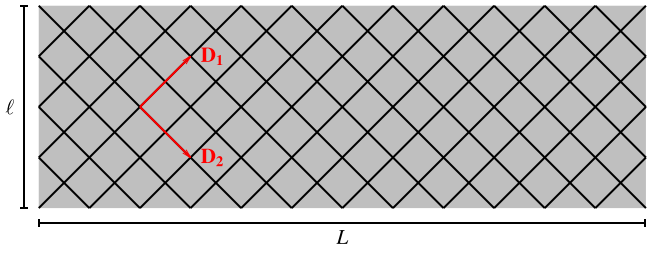

Fig. 10. Reference configuration of the second gradient continuum.

where it is assumed that the thickness of each fiber, b, does not vary or varies negligibly with respect to the variation of the distance h between fiber planes. The overall contraction is therefore of the order of

$$H - H^* = \mathrm{h}\ (n-1)(1-\cos(\vartheta)). \tag{3}$$

3. 2D model accounting for experimental evidences

In his seminal paper, Germain established that, when studying mesostructured continua and given some particular conditions, then the continuum theory to be used is based on a strain energy also depending on the second displacement gradient (Germain, 2020). Even when the meso- and macroscales are not decisively separated, the continuum second gradient model may be used to obtain estimates that are very close to experiments (Spagnuolo et al., 2021).

The second gradient model (dell'Isola et al., 2016; Spagnuolo et al., 2021) is a two-dimensional description, suitable for the characterization of tests that induce strains and stresses only in the plane. Given a placement, which associates each point of the reference configuration to its position in the deformed configuration (Fig. 10 for the adopted nomenclature), an orthogonal basis $(\mathbf{D}_1, \mathbf{D}_2)$ is considered for the reference configuration, oriented along the directions of the two fiber families composing the studied mesostructures.

The mesostructure shown in Fig. 1 is modeled by means of a discrete model where the deformations of the fibers are written in terms of different types of springs. This discrete model is then homogenized for obtaining the continuum strain energy. Let us consider a 2D continuum whose reference shape is given by a rectangular domain $\Omega = [0, L] \times [0, \ell] \subset \mathbb{R}^2$, where L and ℓ are shown in Fig. 10. Very often, it is assumed that $L = 3\ell$. This aspect ratio is generally considered in the literature about pantographic metamaterials (Rahali et al., 2015; Yang et al., 2018; Giorgio et al., 2019; Ciallella et al., 2021, 2022b). Its meaning is due to the fact that, when studying that type of metamaterials, one is mainly interested in the bending of fibers (this deformation mode is related to the second gradient of the placement field in the continuum model) and for observing a pure bending deformation, it is necessary to have at least the $1:3$ ratio. Considering the sample as divided into three squares, only the central zone has sides that are not clamped. In the clamped ends, other contributions must be considered due to the elongation of fibers. Consequently, the minimum aspect ratio for observing "unclamped" bending of fibers is $1:3$. If only planar motions are considered, then the current shape of the rectangle is mathematically described by a regular placement function $\chi : \Omega \to \mathbb{R}^2$. By means of asymptotic homogenization of the mesostructure and assuming that $\chi(\cdot)$ is at least twice differentiable, the macroscopic strain energy obtained by homogenizing the discrete system reads (dell'Isola et al., 2016)

$$\begin{aligned}\mathcal{U}(\chi(\cdot)) = &\int_\Omega \sum_\alpha \frac{\mathrm{K}_e}{2}(\|\boldsymbol{F}\mathbf{D}_\alpha\| - 1)^2\, d\Omega \\ &+ \int_\Omega \sum_\alpha \frac{\mathrm{K}_b}{2}\left[\frac{\nabla\boldsymbol{F}|\mathbf{D}_\alpha\otimes\mathbf{D}_\alpha \cdot \nabla\boldsymbol{F}|\mathbf{D}_\alpha\otimes\mathbf{D}_\alpha}{\|\boldsymbol{F}\mathbf{D}_\alpha\|^2}\right. \\ &\left. - \left(\frac{\boldsymbol{F}\mathbf{D}_\alpha}{\|\boldsymbol{F}\mathbf{D}_\alpha\|}\cdot\frac{\nabla\boldsymbol{F}|\mathbf{D}_\alpha\otimes\mathbf{D}_\alpha}{\|\boldsymbol{F}\mathbf{D}_\alpha\|}\right)^2\right] d\Omega\end{aligned} \tag{4}$$

where $\boldsymbol{F}$ denotes the deformation gradient $\nabla\chi$, and $\left(\nabla\boldsymbol{F}|\mathbf{D}_\alpha\otimes\mathbf{D}_\alpha\right)^\beta = F^\beta_{\alpha,\alpha} = \chi^\beta_{,\alpha\alpha}$. Note that Greek indices assume values in the range 1,2. The first integral in Eq. (4) accounts for the fiber elongation energy (i.e., K_e is the elongation stiffness) while the second integral represents the fiber bending energy (K_b being the bending stiffness). It is worth noting that the bending energy is written in terms of the gradient of the deformation tensor $\nabla\boldsymbol{F}$ corresponding to the second gradient of the placement field $\nabla^2\chi$. In the strain energy (4), no energetic term related to hinges was added. This is the case when hinges are perfect.

When the hinges are not perfect, then one has to take into account their deformations. First, it is necessary to consider their torsion. An energetic term accounting for the torsion of the hinges is obtained by considering the variation of the angle between the two fibers connected by a given hinge. The angle variation corresponds to a torsion of the cylinder (Fig. 11). Following dell'Isola et al. (2016), this energetic term is expressed as

$$\mathcal{U}_s(\chi(\cdot)) = \int_\Omega \frac{K_s}{2}\left|\arccos\left(\frac{\boldsymbol{F}\mathbf{D}_1}{\|\boldsymbol{F}\mathbf{D}_1\|}\cdot\frac{\boldsymbol{F}\mathbf{D}_2}{\|\boldsymbol{F}\mathbf{D}_2\|}\right) - \frac{\pi}{2}\right|^\beta d\Omega \tag{5}$$

where the exponent β is generally taken equal to 2, but should be calibrated on experimental data sets. This energetic term is not able to predict all types of behavior (e.g., for samples manufactured with metals, it has been shown that it does not fit correctly the experimental data (Spagnuolo et al., 2017, 2019; La Valle et al., 2023; Gutmann et al., 2023) but is a good compromise as a first approximation. Moreover, although related to the torsion of the hinges, this energetic term represents, from a macroscopic viewpoint, the shear energy of the pantographic continuum.

Let us note that the discrete structure of considered specimen dictates some material symmetry of the continuum model. In other words, a material anisotropy may play an essential role here. In fact, here we face a kind of cubic symmetry, see *e.g.* (Bertram and Forest, 2020; Bertram, 2023) for the more general discussion of anisotropy in strain gradient continua.

To summarize, one may consider that two continua are introduced for the description of this metamaterial. They are related to the two introduced placement fields, which are employed to describe the displacements of the material points. The need to introduce two continua is related to the fact that this particular metamaterial has a

mesostructure that is seen as an assembly of two fiber families. From a mathematical point of view, the fibers are dense in the sense of a homogenization procedure. The efforts in this direction are based upon the work of Everstine and Pipkin (1973) on inextensible fibers.

3.1. Bending the fibers corresponds to stretching the metamaterial

Thanks to the particular geometry of the meso-architecture of the pantographic metamaterial, with fibers at various levels oriented at a 90 degree angular variation between layers and the fibers being kinematically constrained through hinges, it is observed in a bias extension test that the initial tension in the metamaterial is only associated with fiber bending. This hypothesis is true only if the hinges are perfect. Otherwise, the tensile force measured for a prescribed displacement will be due not only to the bending energy (of the fibers) but also to the torsional (and possibly mesoshear) energy of the hinges. If the hinges are elastic cylinders, their torsional contribution prevails over the bending of fibers, thereby effectively producing a homogenized material where the energy is primarily of the first gradient.

As previously mentioned, in the continuous model, the second gradient energy is due to fiber bending. This observation leads to an important result. The stiffness set of the pantographic metamaterial can be calibrated to have a material governed by either first or second gradient energies. Mathematically, this observation corresponds to a transition from elliptic to hyperbolic solutions.

3.2. Elongation of fibers when the layer misorientation approaches zero

When the relative angles between the various levels of fibers approach values close to zero in the central part of the metamaterial, a phase transition in the behavior of the metamaterial is observed, namely, from a second gradient behavior to a first gradient behavior. This change is due to the activation of the stretching energy of the fibers. The fibers at various levels become fundamentally parallel to each other, and the only way, at the mesoscale, to continue achieving macroscopic elongation is for the fibers themselves to stretch. At this stage, additional deformation mechanisms should be considered. In the present model, terms related to contact between fibers of the same family or mutual sliding, which potentially introduces friction between the fibers, are not considered in the strain energy. These issues were considered by Spagnuolo and Cazzani (2021), Cuomo et al. (2024).

3.3. Mechanics of connecting elements: Hinges

The mechanical behavior of the hinges in pantographic structures plays a key role in determining the overall performance and deformation characteristics of these advanced metamaterials. Hinges act as rotational connectors between the fibers at different levels, allowing for relative motions and energy transfer through bending, stretching, and torsional interactions (La Valle et al., 2024).

In the context of pantographic structures, when the fibers are connected via perfect hinges, the initial deformation under an applied load is primarily due to fiber bending (Cuomo et al., 2017). This behavior aligns with the second gradient elasticity theory, where the energy contributions from bending are significant. However, if the hinges are not ideal and exhibit elasticity themselves, the deformation mechanism changes. The torsional stiffness of the hinges begins to dominate, especially when the fibers are nearly parallel and the angular displacement is minimal (Cuomo et al., 2017). This transition marks a shift from second gradient to first gradient models, where the stretching of the fibers becomes the primary mode of deformation (Cuomo et al., 2017).

Studies have shown that the torsional rigidity of the hinges may significantly influence the mechanical response of the pantographic structure. For example, if the hinges are modeled as elastic cylinders, the torsional energy contribution may overshadow the bending energy of the fibers, effectively transforming the material response from one governed by second gradient effects to one dominated by first gradient effects (Cuomo et al., 2017). This transition is critical for the design and application of pantographic metamaterials, as it allows for the tuning of material properties through the geometric and mechanical characteristics of the hinges and fibers. By understanding and tuning the mechanical behavior of the hinges, one will design pantographic structures with tailored mechanical responses suitable for a variety of applications, from flexible electronics to adaptive architectural components (dell'Isola and Rosa, 1996; Enakoutsa et al., 2017; Eremeyev et al., 2020).

These insights are supported by comprehensive studies and experimental validations (dell'Isola et al., 2016), which explored the coupling between the mesostructural geometry and macroscopic mechanical behavior in pantographic lattices (Carcaterra et al., 2015; Abdoul-Anziz et al., 2019; Fedele, 2022).

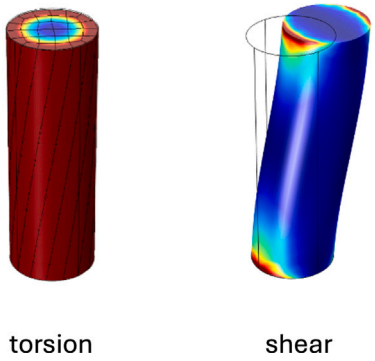

Fig. 11. Kinematics of hinges depicting torsion (left) and meso-shear (right).

3.4. Introduction of mesoshear through field duplication

As previously discussed, different deformation mechanisms occur during the deformation of pantographic metamaterial. Specifically, these deformations affect the constituent elements (*i.e.*, fibers and hinges). For the fibers, they flex or stretch. In particular, the strain energy term related to fiber bending is closely linked, from a theoretical point of view, to the second gradient of the placement field (dell'Isola et al., 2016; Barchiesi et al., 2019; Yang and Müller, 2019; Yildizdag et al., 2020).

As was shown, at least two types of deformation modes are associated with the hinges, namely, torsion and mesoshear. These deformations affect the fibers as relative deformations between the two parallel layers interconnected by the hinges. The torsion of the hinge results in a change in the angle between the fibers, while mesoshear (*i.e.* shear of cylinders) corresponds to the sliding between such fibers (see Fig. 11). While torsion of the hinges always occurs, unless they are perfect, mesoshear of the hinges occurs under certain conditions. The geometry of the connecting hinge determines its torsional stiffness on the one hand (greater rigidity corresponds to thicker cylinders), and its tendency to be sheared on the other hand. It can be established in a rather general way that slender hinges will be easier to be sheared than thicker ones. An example of such a mesoshear deformation mechanism is shown in Fig. 8f.

When mesoshear deformation of the hinges cannot be neglected, the single-field model introduced previously for the description of the pantographic continuum is no longer sufficient to correctly describe the problem at hand. This model must therefore be extended. The simplest way to account for mesoshear and fiber sliding is to adopt not one but two placement fields and to introduce a coupling term. The coupling term represents a measure of mesoshear deformation of the hinges, and the ability of the fibers to slide relative to each other.

From a mathematical point of view, this coupling term is written as

$$U_{ms}(\chi^{\alpha}(\cdot)) = \frac{K_{int}}{2}\int_{\Omega}\left|\chi^{1}-\chi^{2}\right|^{2}\,d\Omega \tag{6}$$

where the integral is intended on the whole region Ω of the continuum, K_{int} is the stiffness related to mesoshear deformation, χ^1 and χ^2 are the two placement fields introduced for taking into account the relative motions of the two fiber families. Once one has included the two fields (χ^1, χ^2) in Eqs. (4)–(5), it is sufficient to add $U_{ms}(\chi^{\alpha}(\cdot))$ to the total energy to obtain a strain energy that describes the pantographic continuum deformation when mesoshear is not negligible.

More in detail, in the case of multilayered structures that are represented as a two-dimensional continuum, two distinct 2D placement fields are introduced to effectively capture the potential interactions occurring between individual fiber layers. This approach allows the relative displacements and deformations of the layers to be accounted for, thereby ensuring for a more accurate description of the structural behavior. The energy formulation given in Eq. (6) is interpreted as a spring-type interaction model, conceptually similar to the one employed in Winkler's foundation model, where the layers are elastically coupled rather than fully bonded. In this context, the fourth stiffness parameter, K_{int}, plays a central role in characterizing the mechanical response of these interlayer interactions. Specifically, K_{int} governs the degree of continuity or relative motion permitted between adjacent fiber layers, influencing the overall stiffness and deformation behavior of the multilayered system.

3.5. On possible fiber contact

Let us note that as for other beam-lattice materials one may observe contact between fibers under certain level of deformation. In this case, additional phenomena related to the contact play even more crucial roles, such as adhesion and other types of interactions. To account for interactions between fibers of the same family, two distinct mechanisms must be considered, depending on the direction of their relative motion, namely, frictional interaction and contact interaction. The frictional interaction may be mathematically modeled by means of a Rayleigh potential, thus representing the energy dissipation due to sliding between fibers. In contrast, the contact interaction enforces the micro-level constraint of impenetrability, preventing fibers from overlapping. Without loss of generality, one may focus on only one family of parallel fibers and introduce a contact energy term that penalizes any reduction in the inter-fiber distance below a critical threshold. This formulation ensures that both dissipative effects of friction and geometric constraint of contact are included in the mechanical description of the metamaterial. Details of this approach can be found in (Spagnuolo and Cazzani, 2021). Hereafter, possible contact was not taken into account.

4. Results

The numerical simulations were conducted using a commercial finite element software, employing Lagrange quadratic shape functions for enhanced accuracy in approximating the deformation fields. Convergence to equilibrium configurations was achieved through a Newton-based iterative solver, ensuring robust treatment of the nonlinear behavior of the system. This computational framework allowed for an efficient and reliable exploration of the model response under various loading conditions.

In order to perform numerical simulations to be compared to experimental analyses, it is necessary to calibrate the constitutive parameters of the model. In this framework, one needs at least two stiffness parameters, namely, K_e and K_b. If it is necessary to include in the description the strain energy due to the torsion of hinges, then a third parameter, K_s, is also included. Last, if mesoshear of hinges is a relevant phenomenon, then K_{int} is to be included as well. These parameters are often referred to as:

Table 2
Initial constitutive parameters before calibration for a single pantographic sheet.

Sample	K_e (N/m)	K_b (N m)	K_s (N/m)
3_w	$1.5 \cdot 10^6$	$0.34 \cdot 10^{-1}$	$7.69 \cdot 10^3$
2_w	$1.5 \cdot 10^6$	$0.34 \cdot 10^{-1}$	$11.53 \cdot 10^3$
2_d	$3.43 \cdot 10^6$	$0.77 \cdot 10^{-1}$	$60.26 \cdot 10^3$

Table 3
Initial constitutive parameters before calibration for a pantographic block.

Sample	K_e (N/m)	K_b (N m)	K_s (N/m)
3_w	$6.75 \cdot 10^6$	$1.53 \cdot 10^{-1}$	$7.69 \cdot 10^3$
2_w	$6.75 \cdot 10^6$	$1.53 \cdot 10^{-1}$	$11.53 \cdot 10^3$
2_d	$15.44 \cdot 10^6$	$3.47 \cdot 10^{-1}$	$60.26 \cdot 10^3$

i. K_e *elongation stiffness*, which is related to the elongation of fibers;
ii. K_b *bending stiffness*, which accounts for fiber bending;
iii. K_s *shear stiffness*, which describes torsion of the hinges;
iv. K_{int} *mesoshear stiffness*, which is related to mesoshear deformation of hinges.

These parameters are to be calibrated by relating numerical simulations with experimental data. The curves of applied force *vs.* prescribed displacement are available for the three specimens. To calibrate the parameters, they are interpreted using the de Saint Venant beam model. The result is an expression written in terms of the geometric properties of the sample. According to the de Saint Venant approach, the constitutive parameters are related to material and geometric characteristics of the specimen as (dell'Isola et al., 2016; Spagnuolo et al., 2017; Abali and Yang, 2019)

$$K_e = \frac{EA}{p}, \quad K_b = \frac{EJ}{p}, \quad K_s = \frac{G\pi r^4}{2hp^2} \tag{7}$$

where E is the Young's modulus, which in the case of polyamide PA2200 is taken equal to $1,600$ MPa, A and J the area and the moment of inertia of the fiber cross-section, G the shear modulus, r and h the radius and height of the hinges, respectively (Table 1), and p the distance between hinges. This distance depends on the fiber density of the specimen (*i.e.,* for specimens 2_w and 3_w, $p = 1.6$ mm, and $p = 0.7$ mm for specimen 2_d).

The fourth parameter, K_{int}, is calibrated once the other three have been obtained. Furthermore, the shear energy (5) has an additional parameter, namely, the exponent β. This exponent was chosen equal to 2 for aluminum alloy samples (Spagnuolo et al., 2017), whereas in the case of polyamide PA2200 samples, $\beta = 1.55$ (Andreaus et al., 2018).

Using formulas (7) the parameters gathered in Table 2 are obtained. The parameters using Eq. (7) are not optimized for printed samples (Table 2), but need to be further scaled. This is understandable when one uses 3D printed specimens that are not fully continuous, but are more granular in nature.

Another aspect must also be taken into account. The parameters obtained in this way refer to a pantographic sheet, whereas the experimental data reported herein refer to a pantographic block. Therefore, in addition to the differences due to 3D printing, which essentially affect the Young's modulus E and consequently the shear modulus G, it is essential to take into account the fact that a pantographic blocks are made up of several pantographic sheets. In the cases under consideration, observing the sections in Fig. 8, each pantographic block corresponds to 4.5 pantographic sheets, so the parameters in Table 2 must be multiplied for this number, at least for the elongation and bending stiffnesses. For the shear stiffness, one should consider that the cylinders of different layers rotate in opposite ways and this compensates the fact that there are different pantographic layers. It is assumed that the shear stiffness of the pantographic block is the same as in the corresponding pantographic sheet. The set of parameters for the pantographic blocks is gathered in Table 3.

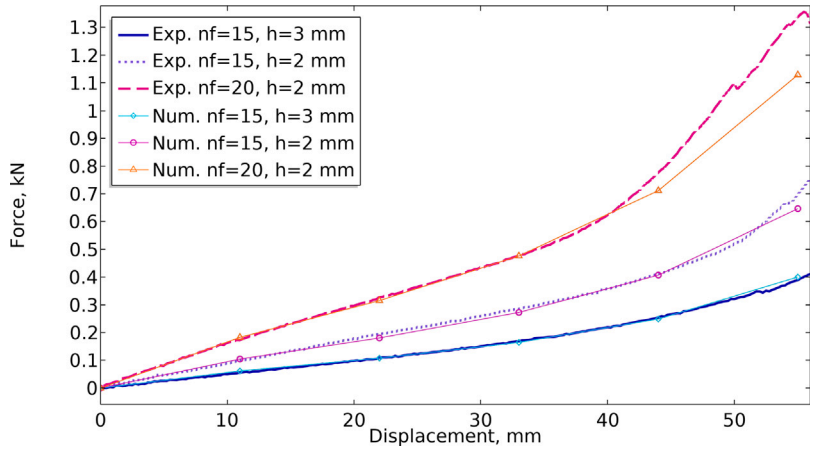

Fig. 12. Comparison between the numerical (Num.) force–displacement curves and the experimental (Exp.) ones.

Table 4
Calibrated constitutive parameters for sample 3_w.

K_e (N/m)	K_b (N m)	K_s (N/m)	K_{int} (N/m^3)
$2.9 \cdot 10^6$	$6.1 \cdot 10^{-1}$	$1.5 \cdot 10^3$	$2.1 \cdot 10^8$

Table 5
Calibrated constitutive parameters.

Sample	K_e (N/m)	K_b (N m)	K_s (N/m)	K_{int} (N/m^3)
3_w	$2.9 \cdot 10^6$	$6.1 \cdot 10^{-1}$	$1.5 \cdot 10^3$	$2.1 \cdot 10^8$
2_w	$2.9 \cdot 10^6$	$6.1 \cdot 10^{-1}$	$2.7 \cdot 10^3$	$3.9 \cdot 10^8$
2_d	$5.1 \cdot 10^6$	$10.7 \cdot 10^{-1}$	$4.6 \cdot 10^3$	$6.7 \cdot 10^8$

Taking into account the considerations about 3D printed materials, which have lower mechanical properties compared to a specimen obtained by melting the same material, the calibrated constitutive parameters of sample 3_w are gathered in Table 4.

Once the constitutive parameters are calibrated for the first sample (3_w), calibrating the other two is easier. Specimens 3_w and 2_w only differ in the height of the hinges, which is no longer 3 mm but 2 mm. Therefore, one only needs to recalibrate the hinge-related stiffnesses K_s and K_{int}, leaving the other two unchanged. It is expected that both hinge-related stiffnesses will be higher. Since the hinges are stiffer, they will be less deformable in torsion and also less susceptible to mesoshear. Last, the constitutive parameters of sample 2_d are directly derived from those of sample 2_w, considering that the two only differ in the number of hinges. If the model is correct, then it is sufficient to divide the parameters of sample 2_w by its total number of hinges and then multiply them by the total number of hinges of sample 2_d.

All calibrated parameters are listed in Table 5. Some parameters, such as the elongation stiffnesses or the shear stiffnesses, are reduced compared to those assumed on the basis of the identification model. However, for the bending stiffness, the calibrated values are higher than the initial assumptions. Further investigations are required to interpret this trend.

The numerical responses of the calibrated model (Table 5) are shown in Fig. 12. There is a very good agreement between the numerical simulations and the experimental data. In the case of specimen 2_d, there is a deviation between the experimental and numerical curves after a prescribed displacements of 40 mm. This divergence is explained by the fact that a greater number of fibers means that they come into contact earlier than in the other cases. The introduced model should therefore be further augmented to take into account contact between fibers of the same family (Spagnuolo and Cazzani, 2021). This effect was not implemented herein.

4.1. About the calibration technique

The calibration of the proposed model generally involves more than simply fitting a single force–displacement curve to the four stiffness parameters. In line with established approaches in the field (dell'Isola et al., 2016), additional experimental data, such as angles between fibers, fiber stretching, and central striction of the specimen, provide multiple distinct curves that significantly enhance the reliability of parameter estimation. Moreover, three of the four parameters are reasonably approximated through standard de Saint-Venant beam theory, leaving only the coupling term between the two fields, namely K_{int}, to be calibrated "from scratch." This approach addresses the inherent nonlinearity of the problem while reducing the overall complexity of the calibration process. By combining force–displacement data with geometric measurements, the uniqueness and comprehensiveness of the parameter estimation are substantially bolstered. In the present case, the model parameters were calibrated solely using force–displacement curves, while acknowledging that the more extensive approach (dell'Isola et al., 2016) would involve additional geometric data. However, the results are in line with what has been shown previously, indicating that this simplified calibration strategy is still qualitatively correct.

Let us discuss the procedure in more detail. The model includes four key material parameters, namely, each parameter governs a different aspect of the structural response, and its calibration follows a logical order based on the observed experimental behavior. First, one calibrates the parameter K_e, which is primarily responsible for stretching that dominates at late stages of the force–displacement curve. It could also be determined by performing experiments on a single fiber. Therefore, K_e was adjusted to ensure a good match between the numerical and experimental responses in that regime, thereby ensuring the correct reproduction of the force increase observed in the later stages of deformation.

Unlike K_s and K_{int}, K_b does not change with the number of hinges, as it is related to the homogenized model properties. It was calibrated by adjusting it to correctly reproduce the curvature observed in the initial segment of the force–displacement curve, where bending deformation dominates before significant stretching occurs (dell'Isola et al., 2015; Cuomo et al., 2016; dell'Isola et al., 2017).

Having K_e and K_b calibrated, one can use the experimental curves for calibration of the other parameters. The parameters K_s and K_{int} are directly influenced by the number of hinges in the metamaterial. As the number of hinges increases, both K_s and K_{int} increase. However, K_{int} is particularly large in the case of stocky hinges since these hinges do not undergo significant shear deformation. The calibration of K_s and K_{int} was performed by iteratively adjusting their values to

match the observed initial stiffness and the transition behavior from bending-dominated to stretching-dominated deformations.

While the calibration was performed using a single experimental curve, additional validation was conducted using the other two curves corresponding to specimens with different geometric characteristics. Importantly, these geometric variations only influence K_s and K_{int}, while K_e and K_b remain unchanged as they are linked to the homogenized model. The consistency of the calibrated parameters across multiple datasets reinforces the validity of the calibrated values.

5. Conclusion

This study presented an in-depth investigation into the mechanical behavior of a metamaterial with a complex mesostructure composed of parallel fibers aligned on different levels. Through a series of bias extension tests on three different pantographic blocks, it was observed that the deformation mechanisms included elongation, bending, and relative sliding between fiber layers. These mechanisms were crucial in the development of the continuum model to predict the metamaterial behavior.

One of the significant findings was the influence of hinge height on the metamaterial response. By normalizing the measured forces with the total number of hinges, it was demonstrated that the metamaterial response was primarily dependent on the hinge height, with similar trends observed for different specimens. This rescaling approach highlighted the key role of the hinges in determining the deformation process of the metamaterial. Further, the rescaling results demonstrated a fundamental behavior of metamaterials. A metamaterial can be understood as a composite material whose properties are essentially determined by its mesostructure rather than by the material properties of its constituents. In the present case, the pantographic metamaterial response is driven by the geometry of the hinges.

The study also revealed the importance of mesoshear deformation, which occurred due to relative sliding between fiber layers. This deformation mechanism became more pronounced in specimens with taller hinges, thereby indicating that slender hinges allow for higher relative displacements between fibers. Additionally, a Poisson-like transverse effect was observed, which was closely related to mesoshear of the hinges and was negligible in specimens with thick hinges.

To describe the observed phenomena, a second gradient continuum model was introduced. This model incorporated energy terms for fiber elongation, bending, and hinge torsion, providing a comprehensive representation of the metamaterial mechanical response. Note that using strain gradient elasticity is essential as this model properly describes a beam-lattice behavior.

Numerical simulations were performed to calibrate the constitutive parameters, and the results showed a good agreement with the experimental data, thereby validating the model.

CRediT authorship contribution statement

M. Spagnuolo: Writing – original draft, Validation, Methodology, Formal analysis, Data curation, Conceptualization. **V.A. Eremeyev:** Writing – review & editing, Supervision, Conceptualization. **F. D'Annibale:** Writing – review & editing, Supervision. **F. Hild:** Writing – review & editing, Writing – original draft, Supervision, Data curation, Conceptualization.

Declaration of competing interest

The authors declare that they have no known competing financial interests or personal relationships that could have appeared to influence the work reported in this paper.

Data availability

Data will be made available on request.

References

Abali, B.E., Yang, H., 2019. Parameter determination of metamaterials in generalized mechanics as a result of computational homogenization. In: D., I., A., K. (Eds.), Advanced Problems in Mechanics. APM 2019. In: Lecture Notes in Mechanical Engineering, Springer, Cham, Swizerland, pp. 22–31.

Abdoul-Anziz, H., Seppecher, P., Bellis, C., 2019. Homogenization of frame lattices leading to second gradient models coupling classical strain and strain-gradient terms. Math. Mech. Solids 24 (12), 3976–3999.

Alibert, J.-J., Seppecher, P., dell'Isola, F., 2003. Truss modular beams with strain energy depending on higher displacement gradients. Math. Mech. Solids 8 (1), 51–73.

Andreaus, U., Spagnuolo, M., Lekszycki, T., Eugster, S.R., 2018. A ritz approach for the static analysis of planar pantographic structures modeled with nonlinear Euler–Bernoulli beams. Contin. Mech. Thermodyn. 30 (5), 1103–1123.

Barchiesi, E., Ganzosch, G., Liebold, C., Placidi, L., Grygoruk, R., Müller, W.H., 2019. Out-of-plane buckling of pantographic fabrics in displacement-controlled shear tests: experimental results and model validation. Contin. Mech. Thermodyn. 31 (1), 33–45.

Bertram, A., 2023. Compendium on Gradient Materials. Springer, Cham.

Bertram, A., Forest, S., 2020. Mechanics of Strain Gradient Materials. Springer, Cham.

Carcaterra, A., dell'Isola, F., Esposito, R., Pulvirenti, M., 2015. Macroscopic description of microscopically strongly inhomogenous systems: A mathematical basis for the synthesis of higher gradients metamaterials. Arch. Ration. Mech. Anal. 218 (3), 1239–1262.

Ciallella, A., Giorgio, I., Eugster, S.R., Rizzi, N.L., dell'Isola, F., 2022a. Generalized beam model for the analysis of wave propagation with a symmetric pattern of deformation in planar pantographic sheets. Wave Motion 113, 102986.

Ciallella, A., Pasquali, D., D'Annibale, F., Giorgio, I., 2022b. Shear rupture mechanism and dissipation phenomena in bias-extension test of pantographic sheets: Numerical modeling and experiments. Math. Mech. Solids 27 (10), 2170–2188.

Ciallella, A., Pasquali, D., Gołaszewski, M., D'Annibale, F., Giorgio, I., 2021. A rate-independent internal friction to describe the hysteretic behavior of pantographic structures under cyclic loads. Mech. Res. Commun. 116, 103761.

Cuomo, M., Contrafatto, L., Greco, L., 2024. A cohesive interface model with degrading friction coefficient. Math. Mech. Complex Syst. 12 (2), 113–133.

Cuomo, M., dell'Isola, F., Greco, L., 2016. Simplified analysis of a generalized bias test for fabrics with two families of inextensible fibres. Z. Angew. Math. Phys. 67 (3), 61.

Cuomo, M., dell'Isola, F., Greco, L., Rizzi, N., 2017. First versus second gradient energies for planar sheets with two families of inextensible fibres: investigation on deformation boundary layers, discontinuities and geometrical instabilities. Compos. Part B: Eng. 115, 423–448.

dell'Isola, F., Cuomo, M., Greco, L., Della Corte, A., 2017. Bias extension test for pantographic sheets: numerical simulations based on second gradient shear energies. J. Engrg. Math. 103 (1), 127–157.

dell'Isola, F., Giorgio, I., Pawlikowski, M., Rizzi, N.L., 2016. Large deformations of planar extensible beams and pantographic lattices: heuristic homogenization, experimental and numerical examples of equilibrium. Proc. R. Soc. A: Math. Phys. Eng. Sci. 472 (2185), 20150790.

dell'Isola, F., Lekszycki, T., Pawlikowski, M., Grygoruk, R., Greco, L., 2015. Designing a light fabric metamaterial being highly macroscopically tough under directional extension: first experimental evidence. Z. Angew. Math. Phys. 66, 3473–3498.

dell'Isola, F., Rosa, L., 1996. Saint venant problem in linear piezoelectricity. In: Smart Structures and Materials 1996: Mathematics and Control in Smart Structures. 2715, International Society for Optics and Photonics, pp. 399–409.

dell'Isola, F., Steigmann, D., 2015. A two-dimensional gradient-elasticity theory for woven fabrics. J. Elasticity 118, 113–125.

Enakoutsa, K., Del Vescovo, D., Scerrato, D., 2017. Combined polarization field gradient and strain field gradient effects in elastic flexoelectric materials. Math. Mech. Solids 22 (5), 938–951.

Eremeyev, V.A., Ganghoffer, J.-F., Konopińska-Zmysłowska, V., Uglov, N.S., 2020. Flexoelectricity and apparent piezoelectricity of a pantographic micro-bar. Internat. J. Engrg. Sci. 149, 103213.

Everstine, G., Pipkin, A., 1973. Boundary layers in fiber-reinforced materials. J. Appl. Mech. 40 (2), 518.

Fedele, R., 2022. Deformation-induced coupling of the generalized external actions in third-gradient materials. Z. Angew. Math. Phys. 73, 218.

Germain, P., 2020. The method of virtual power in the mechanics of continuous media, I: Second-gradient theory. Math. Mech. Complex Syst. 8 (2), 153–190.

Giorgio, I., 2021. Lattice shells composed of two families of curved Kirchhoff rods: an archetypal example, topology optimization of a cycloidal metamaterial. Contin. Mech. Thermodyn. 33 (4), 1063–1082.

Giorgio, I., dell'Isola, F., Steigmann, D.J., 2024. Second-grade elasticity of three-dimensional pantographic lattices: theory and numerical experiments. Contin. Mech. Thermodyn. 36 (5), 1181–1193.

Giorgio, I., Rizzi, N.L., Andreaus, U., Steigmann, D.J., 2019. A two-dimensional continuum model of pantographic sheets moving in a 3D space and accounting for the offset and relative rotations of the fibers. Math. Mech. Complex Syst. 7 (4), 311–325.

Giorgio, I., Varano, V., dell'Isola, F., Rizzi, N.L., 2021. Two layers pantographs: a 2D continuum model accounting for the beams' offset and relative rotations as averages in SO (3) Lie groups. Int. J. Solids Struct. 216, 43–58.

Gutmann, F., Stilz, M., Patil, S., Fischer, F., Hoschke, K., Ganzenmüller, G., Hiermaier, S., 2023. Miniaturization of non-assembly metallic pin-joints by LPBF-based additive manufacturing as perfect pivots for pantographic metamaterials. Materials 16 (5), 1797.

Hild, F., Misra, A., Dell'Isola, F., 2021. Multiscale DIC applied to pantographic structures. Exp. Mech. 61 (2), 431–443.

Hild, F., Roux, S., 2012. Comparison of local and global approaches to Digital Image Correlation. Exp. Mech. 52 (9), 1503–1519.

La Valle, G., Fabbrocino, F., Desmorat, B., 2024. On the influence of microproperties of elastoplastic hinges on the global behavior of pantographic sheets in bias extensional test. Contin. Mech. Thermodyn. 36, 1729–1740.

La Valle, G., Spagnuolo, M., Turco, E., Desmorat, B., 2023. A new torsional energy for pantographic sheets. Z. Angew. Math. Phys. 74 (2), 67.

Laudato, M., Manzari, L., Göransson, P., Giorgio, I., Abali, B.E., 2022. Experimental analysis on metamaterials boundary layers by means of a pantographic structure under large deformations. Mech. Res. Commun. 125, 103990.

Leonardi, S., Dupuy, C., Peyre, P., Helbert, A., Tarantino, M., 2024. Architected metallic cellular materials with random pore features: computer design, LPBF fabrication and mechanical properties. Procedia Struct. Integr. 53, 327–337.

Mindlin, R.D., 1965. Second gradient of strain and surface-tension in linear elasticity. Int. J. Solids Struct. 1 (4), 417–438.

Nadler, B., Steigmann, D.J., 2003. A model for frictional slip in woven fabrics. Comptes Rendus Mec. 331 (12), 797–804.

Rahali, Y., Giorgio, I., Ganghoffer, J., dell'Isola, F., 2015. Homogenization à la piola produces second gradient continuum models for linear pantographic lattices. Internat. J. Engrg. Sci. 97, 148–172.

Seppecher, P., Alibert, J.-J., dell'Isola, F., 2011. Linear elastic trusses leading to continua with exotic mechanical interactions. J. Phys.: Conf. Ser. 319 (1), 012018.

Spagnuolo, M., Barcz, K., Pfaff, A., dell'Isola, F., Franciosi, P., 2017. Qualitative pivot damage analysis in aluminum printed pantographic sheets: numerics and experiments. Mech. Res. Commun. 83, 47–52.

Spagnuolo, M., Cazzani, A.M., 2021. Contact interactions in complex fibrous metamaterials: a proposal for elastic energy and Rayleigh dissipation potential. Contin. Mech. Thermodyn. 33 (4), 1873–1889.

Spagnuolo, M., Peyre, P., Dupuy, C., 2019. Phenomenological aspects of quasi-perfect pivots in metallic pantographic structures. Mech. Res. Commun. 101, 103415.

Spagnuolo, M., Yildizdag, M.E., Andreaus, U., Cazzani, A.M., 2021. Are higher-gradient models also capable of predicting mechanical behavior in the case of wide-knit pantographic structures? Math. Mech. Solids 26 (1), 18–29.

Steigmann, D.J., dell'Isola, F., 2015. Mechanical response of fabric sheets to three-dimensional bending, twisting, and stretching. Acta Mech. Sin. 31, 373–382.

Tomicevic, Z., Hild, F., Roux, S., 2013. Mechanics-aided digital image correlation. Strain Anal. 48, 330–343.

Yang, H., Ganzosch, G., Giorgio, I., Abali, B.E., 2018. Material characterization and computations of a polymeric metamaterial with a pantographic substructure. Z. Angew. Math. Phys. 69 (4), 105.

Yang, H., Müller, W.H., 2019. Computation and experimental comparison of the deformation behavior of pantographic structures with different micro-geometry under shear and torsion. J. Theoret. Appl. Mech. 57.

Yildizdag, M.E., Barchiesi, E., dell'Isola, F., 2020. Three-point bending test of pantographic blocks: numerical and experimental investigation. Math. Mech. Solids 25 (10), 1965–1978.